Nanoscale

Accepted Manuscript

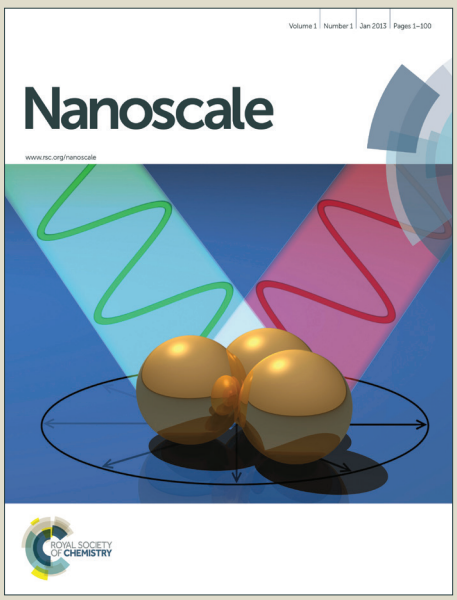

ROYAL SOCIETY OF CHEMISTRY

www.rsc.org/nanoscale

Nanoscale

RSCPublishing

ARTICLE

Quantum dot multiplexing for the profiling of cellular receptors

Cite this: DOI: 10.1039/x0xx00000x

Felipe T. Lee-Montiel[a], Peter Li[b], PI. Imoukhuede[a†]

Received ooth January 2012,
Accepted ooth January 2012

DOI: 10.1039/x0xx00000x

www.rsc.org/

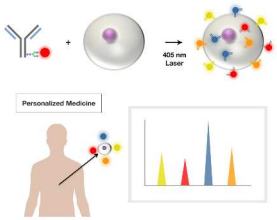

Multicolor Quantum dots multiplexing single cell analysis of membrane receptors for the development of better patient therapies and the advance of personalized medicine.

The profiling of cellular heterogeneity has wide-reaching importance for our understanding of how cells function and react to their environments in healthy and diseased states. Our ability to interpret and model cell behavior has been limited by the difficulties of measuring cell differences, for example, comparing tumor and non-tumor cells, particularly at the individual cell level. This demonstrates a clear need for a generalizable approach to profile fluorophore sites on cells or molecular assemblies on beads. Here, a multiplex immunoassay for simultaneous detection of five different angiogenic markers was developed. We targeted angiogenic receptors in the vascular endothelial growth factor family (VEGFR1, VEGFR2 and VEGFR3) and Neuropilin (NRP) family (NRP1 and NRP2), using multicolor quantum dots (Qdots). Copper-free click based chemistry was used to conjugate the monoclonal antibodies with 525, 565, 605, 655 and 705 nm CdSe/ZnS Qdots. We tested and performed colocalization analysis of our nanoprobes using the Pearson correlation coefficient statistical analysis. Human umbilical vein endothelial cells (HUVEC) were tested. The ability to easily monitor the molecular indicators of angiogenesis that are a precursor to cancer in a fast and cost effective system is an important step towards personalized nanomedicine.

Introduction

Plasma membrane receptors are the initial transducers of extracellular signaling towards an intracellular response, which depends on the quantity and distribution of these receptors [1]. As such, the regulation of plasma membrane receptors and transporters has been extensively studied with focus on protein clustering and assembly [2, 3], oligomerization [4-6], and protein-protein interactions [7, 8]. Here we examine the vascular endothelial growth factor (VEGFR) family, which is critical to angiogenesis. The accurate quantification of biological levels of VEGFR is a limiting step in understanding the mechanisms of blood vessel formation and in the development of disease treatments related to angiogenesis. Indeed, VEGFRs serve as angiogenic biomarkers [9-11] and gaining a quantitative understanding of these biomarkers will enhance our understanding of breast cancers and several other pathologies. Towards these goals, we have recently established the optimal conditions for quantitative flow (qFlow) cytometry profiling of VEGFRs. This allowed for quantitative profiling of endothelial plasma membrane VEGFR in vitro [12, 13] normal mouse tissue *ex vivo* [14], ischemic mouse tissue *ex vivo* [15], and breast cancer xenografts, *ex vivo* [16]. The data obtained from these profiling studies have advanced systems biology models of tumor angiogenesis [17-20]. These studies also established a new method for quantitative characterization of the tumor microenvironment and how it changes with tumor development.

Fluorescence-based methods offer plentiful options for quantitative characterization of cells and tissue[21-24]. However, many approaches have applied organic fluorophores, which have broad emission spectra. The advancement of quantum dot (Qdot)-based quantitative fluorescent technology could provide multiplexing capabilities to simultaneously detect numerous biomolecules, improving receptor-mapping technology. Qdots are single nanocrystals that exhibiting several favorable properties; most notably, when excited they emit within a narrow, largely symmetric range, allowing multiple Qdots to be monitored simultaneously [25, 26]. Qdots are commercially available with many surface modifications for a wide range of applications. Qdots particles absorb photons at high energy and emit at longer wavelength, with the emission being affected by their size and shape as well as their chemical properties. Their physical dimensions affect the brightness and color of Qdots, with the peak emission wavelength being approximately proportional to the square of size of the core of the nanocrystal [27 28]. Additionally, Qdots are 100-times more resistant to photobleaching than organic fluorophores, and they have a much brighter signal, making them much more effective than traditional fluorescent detection methods [29]. For this study, we employed five different commercially available Qdots composed of cadmium-selenium (CdSe) core, zinc sulfide (ZnS) shell and a surface coating of polyethylene glycol that helps to prevent non-specific binding. The Qdots chosen were 525, 565, 605, 655 and 705 nm emission spectra.

Qdots are ideal tools for multiplexing, and recently, significant strides have been made towards this goal. The unique optical properties of Qdots combined with their spatial resolution have already lead to improvements in some existing diagnostic assays. Qdots have allowed simultaneous imaging of eight Qdot-coupled peptides and antibodies[30]. In addition, Qdot-immunolabeling of breast and lung cancer cell lines has enabled more sensitive early cancer biomarkers[31]. Yezhelyev et al[32] pioneered Qdot-enabled comparison of HER2, ER, and PR expression, towards multiplexed Qdot quantification. To our knowledge, Qdots have not been multiplexed to profile and assess the colocalization of angiogenic receptors.

Here we present the simultaneous nanosensing of the angiogenic receptors VEGFR1, VEGFR2, VEGFR3, NRP1, and NRP2 using Qdots. We applied a copper-free antibody conjugation approach using Site Click chemistry and determined the labeling ratio of nanosensors. We also quantified the cytotoxicity of the Qdot conjugates and determined the optimal fixation and live cell conditions for imaging of the Qdot-based nanosensors. The development of these nanosensors provides new insight into key receptors mediating angiogenesis, while advancing the use of Qdot probes for multicolor imaging.

Results and Discussion

Our study shows how confocal fluorescence microscopy can be used to quantitatively and qualitatively assess the distribution of and interaction between a ligand and its receptor. The present work involved tagging potential interacting partners with distinct fluorophores, in this case five different Qdots to achieve a multiplex staining of the cells. We analyzed the data using ImageJ-FIJI to compare the fluorescence intensity of two antibody-conjugated Qdots at each pixel in a two-channel image combination, which helped to reveal regions of colocalization.

Qdot-Ab conjugation SMCC

We conjugated Qdots to monoclonal antibodies using the SMCC based antibody conjugation kit. This approach requires reduction of the IgG, which fractionates the heavy and light chains of the IgG. Next an amine-thiol bond is formed between light chains (antibody region with antigen recognition sites) and the Qdots (Supplemental Figure S1-A). After conjugation, we quantified the Qdot-antibody conjugation ratio, using a reducing gel (SDS-PAGE) to liberate the conjugated light chains.

Qdot-Ab conjugation Siteclick

Since conjugation of Qdots to light chains may affect antigen binding, we tested a second conjugation approach: Copper-free click chemistry. This method relies on the cleavage of the galactose carbohydrate groups using a glycoside hydrolyse enzyme (galactosidase) on the Fc antibody domain (Supplemental figure S1-B), thus maintaining the integrity of the antigen binding site. After its modification, an azide containing sugar was added to the modified carbohydrate

domain of the antibody. Finally, the modified antibody was conjugated to the Qdot via the dibenzocyclooctyne (DIBO) molecule located on the surface of the Qdot. We similarly quantified and calibrated antibody-Qdot conjugation with a reducing gel. Prior to purification of Qdot-antibody product, a ratio of 4:1 IgG antibodies to Qdots was observed (Supplemental Figure S2). Our calculation of only one Qdot per four IgG is likely due to the lack of the purification step to remove the unbound antibodies in the solution. In theory, this conjugation chemistry uses the four carbohydrate chains, found in the Fc domain of the monoclonal antibody. However, there is a potential for steric hindrance in the antibodies as two of the carbohydrate chains are close to each other on each side, which may have reduced the available number of Qdots binding sites to two.

Qdot sizing and geometry

Our functionalization can affect the overall avidity of the nanosensor complex to target/cell receptors [33]. Dynamic light scattering was used to determine the size of the entire Qdot-antibody conjugate. We observed average size variations between 16-21 nm (Supplemental Figure S3). TEM images (Supplemental figure S4) showed that the non-conjugated part of the Qdots have a size difference of 5-11 nm due to the polyethylene glycol (PEG layer), aqueous layer and IgG bound to the Qdots not measured with the TEM technology [34-36]. We observed that the QD525-anti-VEGFR1 conjugate had the smallest average size (~16 nm) and the QD705-anti-NRP2 conjugate had the largest average size (~21 nm). We also observe an increased standard error when measuring the larger particles (QD605, QD655, & QD705) possibly due to differential light scattering about their non-spherical axes. The similarity in size across antibodies indicates that the Qdot size-emission wavelength scaling, QD525 < QD565 < QD605 < QD655 < QD705 (Supplemental Figure S3), which we previously reported [37], is preserved following Qdot-antibody conjugation. Sizing and geometry remain important aspects of nanosensor development. In particular, Qdot size can markedly affect translocation of particles through gap junctions [38] and cause multivalent Qdot aggregation [39]. Qdot surface functionalization can also affect their lifetime in the bloodstream and bioaccumulation in different organs [40]. Therefore, our quantification of Qdot-antibody size provides insight necessary for their *in vitro* and *in vivo* application.

Stabilizing Qdot cytotoxicity through buffers and supplements

Qdots are known to be cytotoxic [41, 42]. Modification of Qdot surface functionalization and changes in Qdot core composition [43, 44] have been employed to decrease Qdot toxicity. We therefore determined Qdot concentrations and incubation times that elicit significant cytotoxicity. Across three concentration ranges tested (20 nM, 30 nM, and 40 nM) the Qdot (CdSe/ZnS) toxicity generally scaled inversely with size (Figure 1A), and as we have shown, size is proportional to emission wavelength (Supplemental Figure S4-F). Therefore, the smaller, lower wavelength Qdots (QD525) have the highest toxicity and the larger, higher wavelength Qdots (QD705) have the lowest toxicity (Figure 1A). This result is consistent with prior studies, finding that smaller, round Qdots and gold nanoparticles are internalized faster that bigger, rod shape Qdots, which results in faster Cd degradation and faster release of Cd to the cells [45, 46]. The fast toxicity may indicate that the Qdots are disrupting the membrane and causing inflammation[47] as the short exposure time of the experiment may not be enough for significant release of Cd from the core.

The ability of different cell culture buffers to reduce Qdot toxicity was assessed. We tested stain buffer (SB) [48], which is often used to preserve cells in flow cytometry. It is buffered with PBS and contains both BSA, which prevents non-specific binding, and sodium azide, a preservative and metabolic inhibitor [49] that reduces endocytosis via ATP depletion [50-52]. We also tested Lebovitz media (L15), which contains glucose, free base amino acids and is buffered by salts. Both buffers were designed to be used with cells at atmospheric conditions (outside an incubator). Both the SB and L15 buffers decreased cell viability with increased Qdot concentration. However, L15 media preserved cell viability to a greater extent than SB (Figure 1B).

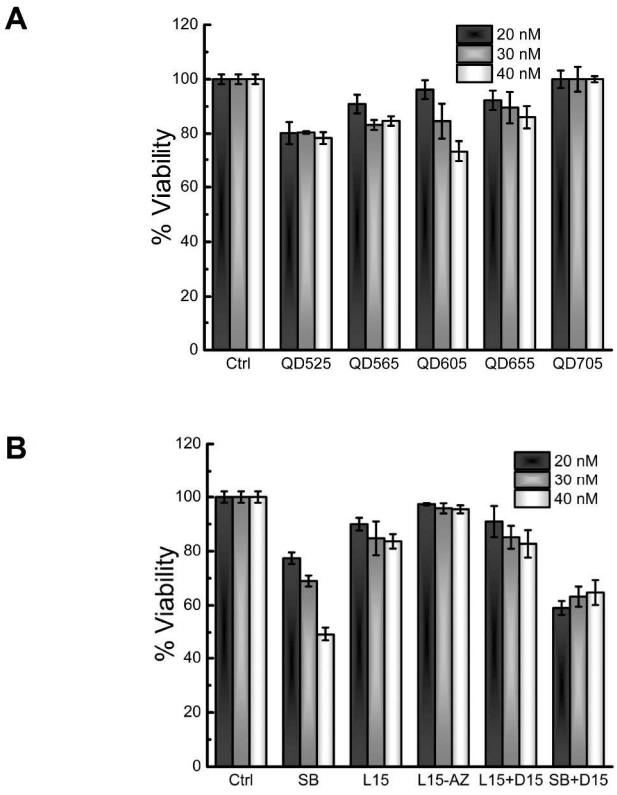

Figure 1. MTT cytotoxicity assay to assess the toxicity of the different Qdots to live cells. (A) Viability of HUVECs incubated with three different concentrations of Qdots (20 nM, 30 nM and 40 nM) showing that Qdots cytotoxicity correlates with lower hydrodynamic diameter Qdots. (B) A reduction in cytotoxicity of Qdot 605 nm to HUVECs was observed when cells were incubated in some cell culture mediums compared to sample buffer, with L15-AZ being the most effective. Control

(Ctrl) samples contain PBS without Qdots and samples in Figure A were analyzed using sample buffer.

As we have described, Qdot cytotoxicity can be attributed to Qdot internalization [53, 54]. Once internalized, Qdots are degraded, releasing the toxic Cd core. However, Cd toxicity is not the only source of Qdot toxicity as there are other factors such as intracellular distribution of Qdots that have associated nanoscale effects [35]. Therefore, we examined the effectiveness of supplementing buffer with either the endocytosis inhibitor D15 [55-57] or the preservative and metabolic inhibitor sodium azide [49]. We observed that sodium azide in the L15 media maintained nearly 100% cell viability, and D15 resulted in a similar viability as L15 alone. D15 added to SB resulted in lower cell viability compared to the addition of SB alone. These data indicate the need to strike a delicate balance between glucose supplementation to sustain cells, and metabolic inhibition to negate Qdot toxicity.

Optimizing cellular fixation for Qdot-cell analysis

Although live cell imaging is the ideal approach for visualizing cell processes, fixation offers the option of preserving cellular state for later analysis. A previous study by Williams et al. [58] showed that labeling epithelial and monocyte cell lines with similar (CdTe) Qdots prior to fixation with high paraformaldehyde (PFA) concentrations (3-4%) caused significant decreases in fluorescence intensity when compared to non-fixed cells. While 1-2% PFA labeling may preserve fluorescence, 1% PFA may decrease nuclear size [58]. Therefore, we extend an analysis of fixation to HUVECs. First, we examined the effect of PFA concentration on HUVEC structure. Using 1% or 2% formaldehyde for 15 minutes resulted in cell rounding and decreased cell adherence to substrate (Figure 2A-B). 1% PFA fixation also caused a notable reduction in nuclear size, in contrast to 2% and 3% solutions, which both equally maintained nuclear integrity (Figure 2B & 2C). The 1% PFA-induced decrease in HUVEC nuclear diameter (Figure 2F) is consistent with prior studies on epithelial cells and monocytes [58]. 3-4% formaldehyde preserved the cells more successfully (Figure 2C and 2D), so we applied high (4%) PFA for HUVEC fixation.

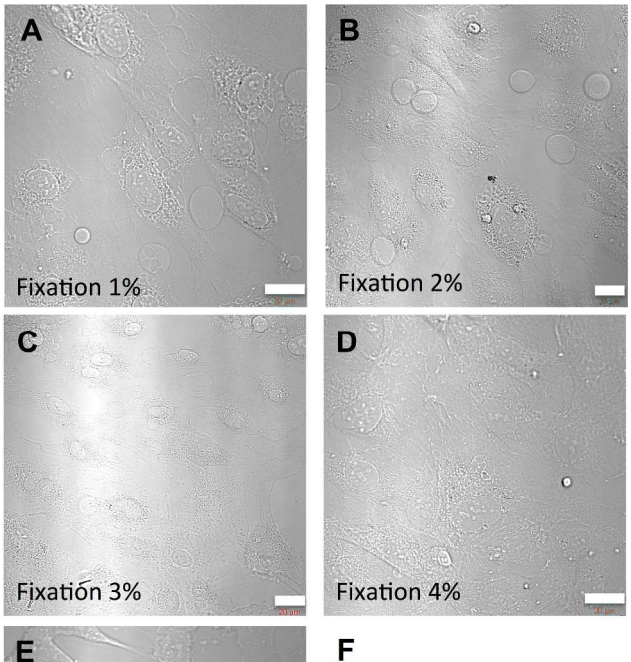

Figure 2. Comparison of the cell monolayer structure of HUVECs fixed with 1%, 2%, 3% and 4% formaldehyde for 15 min (A-D) and live condition (E). Images acquired using transmission PMT. The effects of the use of 1% and 2% formaldehyde in the nuclear structure are shown in (F) and lifting of the cell monolayer over time can be seen in (A-C). Scale bar represents 20 µm.

We also examined how fixation affects fluorescence, observing that HUVEC Qdot labeling followed by fixation resulted in lower Qdot fluorescence intensities (Figure 3) compared to fixing first then labeling (Figure 4). Quantification of the fluorescence intensity change between the two protocols showed a ~90% reduction in fluorescence levels (Figure 5), which is consistent with prior studies for CdTe Qdots on epithelial cells and monocytes [58]. Therefore, HUVEC fixation should occur prior to Qdot labeling.

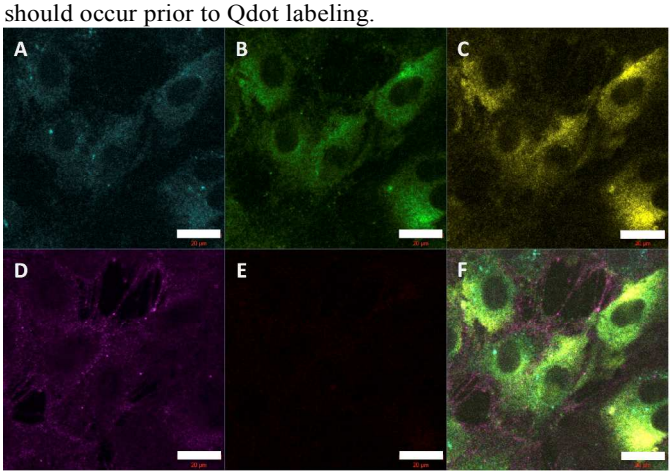

Figure 3. Confocal image of HUVECs labeled with (A) Qdot 525-VEGFR1, (B) Qdot 565-VEGFR2, (C) Qdot 605-VEGFR3, (D) Qdot 655-NRP1 and (E) Qdot 705-NRP2 and (F) Merged image (A-E). Cell monolayers were Qdot-labeled for 45 min then fixed with 4% paraformaldehyde for 15 min at room temperature. Scale bar represents 20 µm.

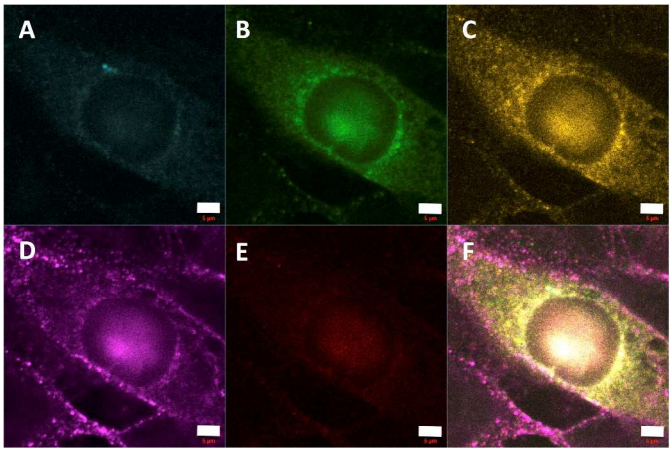

Figure 4. Confocal image of a single HUVEC previously fixed with 4% paraformaldehyde and simultaneously stained with

five different antibody conjugated Qdots. (A) Qdot 525-VEGFR1 (B) Qdot 565-VEGFR2, (C) Qdot 565-VEGFR2, (D) Qdot 605-VEGFR3, Qdot 655-NRP1 and (E) Qdot 705-NRP2. (F) Merged channels. VEGFR1 had the lower fluorescence level and the strongest fluorescence signal was for NRP1, which correlates with the higher number of receptors. Scale bars represent 5 µm and the resolution used with the confocal microscope was 100 nm.

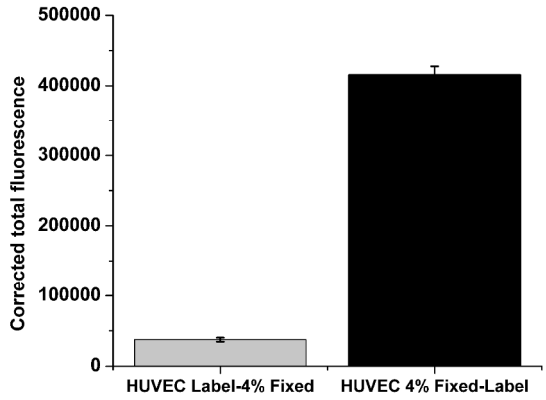

Figure 5. Corrected total cell fluorescence (CTCF) intensity measurements of HUVECs labeled with NRP-1-Qdot655 then fixed with 4% PFA and HUVECs fixed with 4% PFA and then labeled. The fluorescence intensity change between these two protocols was 89.5 %. Fixing the cells first resulted in higher fluorescence intensity than labeling first then fixing.

Analysis of VEGFR cellular localization and co-localization

As observed in Figures 3 and 4, the three membrane-localized VEGFRs: VEGFR1, VEGFR2, & VEGFR3 along with their co-receptors, NRP1 and NRP2, were successfully labeled and visualized in HUVEC and HDFa cell lines (Supplemental figure S5) using Qdot-nanosensors. We next mapped their spatial organization and relative levels of surface presentation. VEGFR1 displayed very low plasma membrane fluorescence, while VEGFR2, VEGFR3, and NRP1 showed much stronger membrane labeling. This is consistent with our prior quantitative analysis, showing less than 2,000 VEGFR1/HUVEC [12]. We also observed significant intracellular VEGFR1 localization, which is consistent with studies identifying ~80% of total VEGFR1 localization [59, 60].

VEGFR2 displayed somewhat uniform partitioning across the membrane, cytoplasmic and nuclear compartments, which is consistent with prior studies reporting 40% of total VEGFR2 residing intracellularly[59, 61-66], with constant VEGFR2 trafficking to the plasma membrane [65] and to the nucleus [60]. We observed significant VEGFR3 localization in three compartments: plasma membrane, cytoplasm, and nucleus.

We primarily observed NRP1 labeling on the plasma membrane and we observed low, NRP2 labeling, primarily localized to the nucleus. Neuropilins are transmembrane proteins and serve as co-receptors of the VEGFRs [67]. Our prior studies showed NRP1 presence *in vitro* on human macrovascular blood endothelial cells, human dermal microvascular endothelial cells, and human dermal lymphatic microvascular endothelial cells at surface levels >30,000/endothelial cell. Therefore, the strong membrane labeling observed with NRP1 is consistent with our prior data [12] and consistent with several studies describing its localization on endothelium [68, 69].

Although NRP2 is expressed in HUVECs [70], the low-NRP2 staining observed may seem inconsistent with its role in both VEGF [71] and class 3 semaphorin [72] signal transduction; however, there are studies describing lower presence on blood-endothelium. Post-embryonically, NRP2 shows low venous staining [73] and high lymphatic staining [74, 75]. NRP2 is also found on osteoclasts [76], and given the role of NRP2 in CNS development, it is also highly localized to midbrain dopaminergic neurons [77] and several cell types throughout the brain, including: microglia, meningeal fibroblasts, and astrocytes [78]. Therefore, the low-NRP2 staining we observed may suggest a decreased role in post-embryonic blood endothelium.

The cellular localization of Neuropilins is an area of interest, given their expression by a variety of tumors and metastases [79], and their role in mediating tumor growth and invasion [80, 81] with a recent study showing that NRP1 can suppress angiogenesis by presenting VEGF to VEGFR2 in trans-conformation (across-cells) while promoting angiogenesis via its role as a co-receptor of VEGFR2 on the same cell [69]. Our multilabeling also provides insight receptor colocalization (Figure 6).

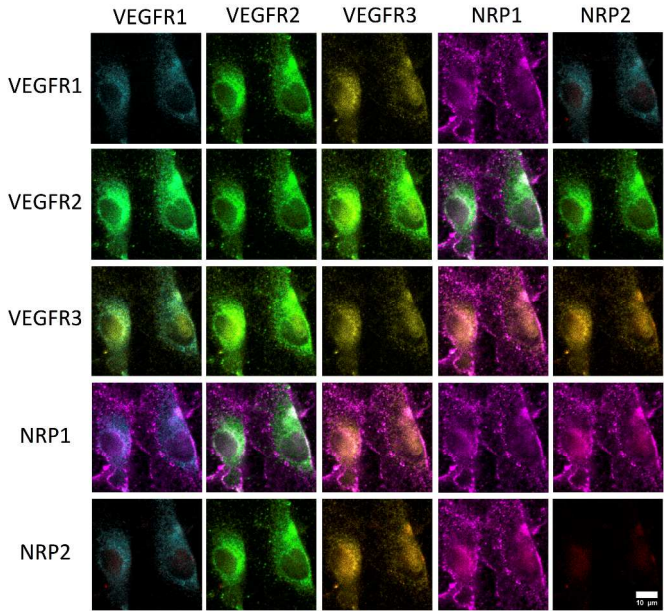

Figure 6. Multiplexed one-step staining of fixed HUVEC cells with Qdot-antibody probes. Colocalization analysis of the different receptors combinations was performed using the FIJI software package. Each image square shows the cells labeled with Qdots in two fluorescent channels binding to the receptor combination listed in the row and column names (left and top).'

The co-localization analysis reported in Table 1 measured the fraction of overlapping signals in images of two distinct fluorescent probes bound to two different cell surface receptors. A significant overlap in the intensity of signal from the two channels in a given pixel indicates colocalization of the receptors. The linear correlation between the intensity of signals from the two channels at every pixel was measured using the Pearson's Coefficient (PC) [82]. PC values range from -1 to 1, with 0 indicating random overlap, 1 perfect co-localization and -1 mutually exclusive localization. A PC greater than 0.5 indicates colocalization and PC less than or equal to 0 indicates random overlap. These intensity measures have the advantage of being independent of brightness and not influenced by constant background, but can be less accurate or difficult to interpret for signals that are not highly correlated or have high noise. In some images with different distribution of binding partners it can be difficult to distinguish overlapping pixels from background noise, therefore, a threshold level is used. Costes et al. [83] developed a statistical evaluation of PC significance, whereby the pixels are scrambled and 100 randomized images assessed to give a 95% confidence threshold for each image, in addition to calculations of relative objective intensity thresholds for each image. The Costes approach has the advantages of automatic threshold and statistical significance calculations, which minimize the influence of noise but require more computational power.

VEGFR1-R2, VEGFR2-R3, and VEGFR2-N1 receptor pairs showed >60% colocalization. The VEGFR1-R2 colocalization is consistent with prior studies reporting their heterodimerization: with a functional role of modulating VEGF activity. Such VEGFR1-R2 heterodimerization may negatively regulate angiogenesis, endothelial cell growth and homeostasis [84-86], and tumor growth [87] by reducing the numbers of pro-angiogenic VEGFR2 homodimers [88]. Additionally, VEGFR1-R2 heterodimers increase the migration of porcine aortic endothelial cells (PAEs) towards VEGF-A_{165}, compared to PAEs expressing VEGFR2 alone [85, 89-92]. On the endothelial cell surface *in vitro*, VEGFR1 can be up to ten-fold less abundant than VEGFR-2 [87, 93], so it is has been predicted to primarily exist in a heterodimeric state with VEGFR-2 [88]. The heterodimerization between VEGFR2-R3 has a functional role of modulating angiogenic sprouting [94-96], while the heterodimerization between VEGFR2-N1 can result in a 4 to 6-fold enhancement in cellular chemotaxis and binding of VEGF-A_{165} to VEGFR2, thereby mediating the proliferation and migration progression within angiogenesis [97, 98].

Receptor combination	Percent of images positive for colocalization (of 5 images per receptor combination)		Conclusion: Colocalization = Yes No colocalization = No
	Pearson Coefficient >0.5 (no threshold)	Pearson Coefficient >0.5 (Costes threshold)	
R1R2	100%	80%	Yes
R1R3	60%	20%	Yes
R1N1	20%	0%	No
R1N2	0%	0%	No
R2R3	100%	100%	Yes
R2N1	60%	60%	Yes
R2N2	0%	0%	No
R3N1	40%	40%	Yes
R3N2	20%	0%	No
N1N2	20%	0%	No

Table 1. Colocalization analysis of confocal images**.** Five random images were analyzed for each receptor combination . The values show the percentage of the five cell slices that were positive for colocalization using the Pearson Coefficient (PC).

Colocalization of VEGFR1-R3 was observed in 60% of images analyzed with PC examination alone and 20% of images when thresholded. VEGFR3-N1 colocalization occurs in 40% of both thresholded and unthresholded images, however, this does not preclude the possibility of complexes containing VEGFR1-R3 or VEGFR3-N1. Indeed, given that VEGFR2-R3 heterodimerize and N1 is a co-receptor of VEGFR2, it is possible that a VEGFR2-R3-N1 complex may exist. Similarly, several receptors are known to cluster on the plasma membrane [2, 7] and colocalize with caveolae/lipid rafts [99]. VEGFR2 has been shown to colocalize with caveolin [100] and disruption of lipid rafts inhibits VEGF-A mediated p38 signaling [101]. Given the presence of VEGFR1-R2 heterodimerization, it is likely that some VEGFR1 may be present on a VEGFR2-R3 raft. Example HUVEC images show how the levels of JACOB thresholded (Figure 7) and Costes automatic threshold (Figure 8) affect the colocalization analysis of the angiogenic receptor pairs. Images show pixels in green for channel 1 and red for channel 2, while white pixels represent the colocalization of the two channels.

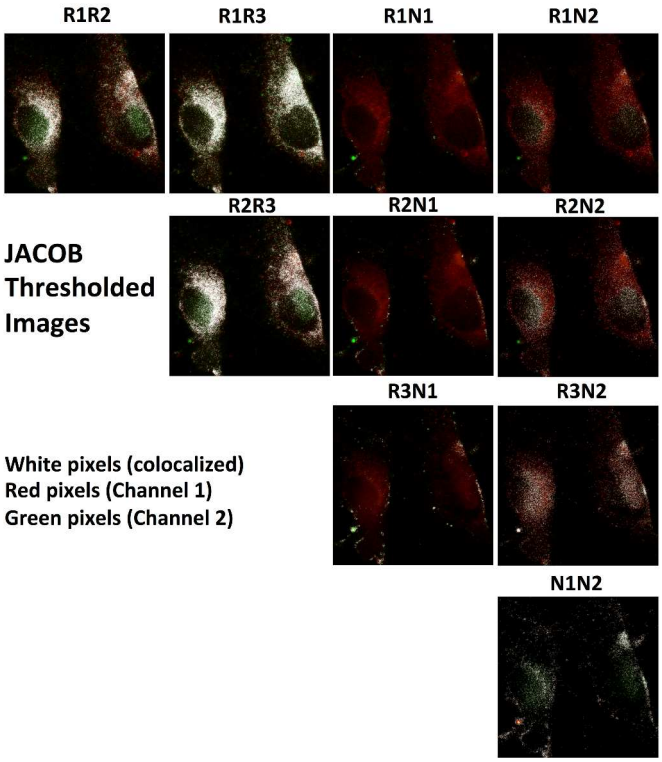

Figure 7. HUVEC showing colocalized pixels using JACOB software to analyze the different colocalization values of the QD525-VEGFR1, QD565-VEGFR2, QD605-VEGFR3, QD655-NRP1 and QD705-NRP2.

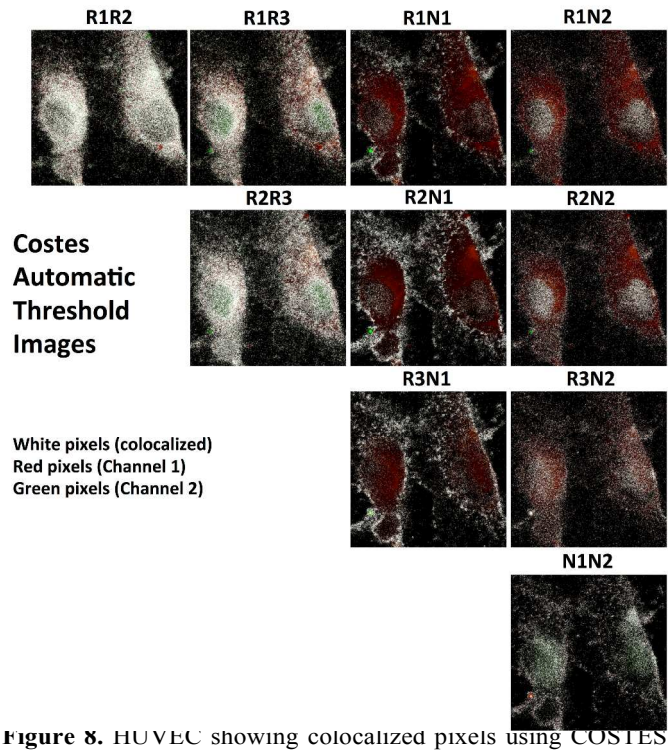

Figure 8. HUVEC showing colocalized pixels using COSTES Automatic threshold to analyze the different colocalization values of the QD525-VEGFR1, QD565-VEGFR2, QD605-VEGFR3, QD655-NRP1 and QD705-NRP2.

Although the co-localization suggests receptor interactions, it is important to consider method limitations, including resolution noise, and the use of fixed cells. The numerical aperture (NA) limits resolution, here to an estimated maximal resolution of 0.1 μm for the x and y axes and 0.2 μm for the z axis, giving a minimum voxel volume of ≥ 0.002 μm^3. These resolution limits may explain the ambiguous results obtained for some receptor interactions in the analysis of the z-stack image (Table S7). It is unlikely that these ambiguities are due to interference among the fluorescence of the five different Qdots, as experiments using fewer numbers of Qdots obtained the same results (data not shown). Automated thresholding and variable stoichiometry of red to green channels can also add noise to data.

The distance required for interactions to occur between two receptors is 40-50 nm [102] The microscope we used has a resolution of 100nm in the X and Y axes and therefore cannot resolve monomers or dimers due to the diffraction limit. While we cannot see individual receptors, we are likely to see microdomains/lipid rafts/caveolin-rich domains. VEGF receptors can have a highly heterogeneous distribution with small areas of high density [103, 104]. For T-cell receptors, these protein islands are 70–140 nm in diameter [104]. . While the colocalization of receptors observed in fixed cells could indicate dimerization, live cells would need to be used to explore these dynamics. These interactions could be better resolved using methods such as Förster Resonance Energy Transfer (FRET)[4], yeast two-hybrid, or co-immunoprecipitation. Furthermore, it is unlikely given the small Qdot-antibody probes (~20nm, that they are causing the colocalization by recruiting receptors, as occurs for larger particles (>50nm) [105, 106].

Experimental

Cell Culture. Human umbilical vein endothelial cells (HUVEC) were acquired from individual donors (Life technologies, Carlsbad, CA and Stem Cell Technologies, Vancouver, Canada). Endothelial cells were maintained in Endothelial Cell Growth Medium-2 (EGM-2), supplemented by the EGM-2 SingleQuot Kit for HUVECs (Lonza, Walkersville, MD), and were used only until passage number 6. Cells were grown at 37°C in 95% air, 5% CO_2. For routine cell culture, cells were detached from flasks using 0.25% TrypLe (Life technologies).

Quantum Dots. We used five different Qdots CdSe/ZnS nanocrystals with 525, 565, 605, 655 and 705 nm emission (Invitrogen, Carlsbad, CA). We tested two different Qdot-antibody conjugation kits which both have the SSMC chemistry catalog number: Q22041MP, Q22031MP, Q22001MP, Q22021MP, Q22061MP and copper free click chemistry catalog numbers: S10449, S10450, S10469, S10453, S10454.

Quantifying Qdot Cytotoxicity via MTT. Newly confluent cell monolayers were trypsinized, resuspended in EGM-2 medium, seeded at 18,000-20,000 cells per well into NUNC delta treated 96-well plates (Thermo, Waltham, MA), and covered with 200 μL of media per well. Cells are incubated for 24 h to allow cell attachment and growth then exposed to increasing concentrations of Qdots for 1 h. Cellular metabolism is evaluated using an MTT (3(4,5-dimethylthiazol-2-yl) 2,5-diphenyltetrazolium bromide) assay (Invitrogen, Carlsbad, CA). A 5 mg/mL MTT solution is dissolved PBS via sonication. A 10% MTT-cell media solution (100 μL) is added to each well of a 96-well plate and incubated at 37 ºC for 4 h. The solution is aspirated, and 100 μL of DFD-HCL solution is added to dissolve the crystalline formazan product. Absorbance is measured at 570 nm on a Synergy HT multiwell plate reader (Biotek, Winooski, VT).

Qdots-Antibody conjugation. Qdots are conjugated to monoclonal antibodies for VEGFR1, VEGFR2, VEGFR3, NRP1 and NRP2 antibodies (R&D Systems, Minneapolis, MN) with Cadmium selenide/Zinc sulphide Qdots 525, 565, 605, 655 and 705 nm, respectively using two different conjugation chemistries: SMCC and Copper-free Click.

SMCC Qdots-Antibody Conjugation kit. SMCC Qdot Antibody Conjugation Kits contain amine-derivatized, PEG-coated nanocrystals and the amine-thiol crosslinker, SMCC. The polymer shell (PEG) of the Qdots contains amine groups, which allow the materials to be conjugated to biological molecules and to retain their optical properties. Qdots are activated with SMCC, yielding a maleimide-nanocrystal surface. Antibodies are reduced and fragmented with DTT to expose free sulfhydryls, and excess SMCC and DTT are

removed by size exclusion chromatography. Activated Qdots are covalently coupled with reduced antibody and the reaction is quenched with β-mercaptoethanol. The 1:1 molar ratio of antibody fragments to the Qdots at mixing is achieved by modifying the amount of antibody added to the Qdots. Conjugates are concentrated by ultrafiltration and purified by size exclusion chromatography.

Copper-free click Antibody conjugation kit. The Copper-free click conjugation consists of three steps: antibody carbohydrate domain modification, azide attachment to the antibody, and conjugation with the DIBO-modified label. It relies on copper-free click chemistry to covalently link the label containing the dibenzocyclooxtyne (DIBO) moiety with the azide-modified antibody without reducing the protein. The molar ratio of antibody fragments to the Qdots at mixing is ~3:1. Conjugates are concentrated by ultrafiltration. In both conjugation chemistries, antibody-Qdot complex SDS-PAGE is performed to quantify the light chain band.

Confocal Imaging. 8 x 10^4 cells/well are seeded on 8-well coverglass (Thermo Biotek I, Biotek II) and incubated for 24 h at 37 °C to allow for cell attachment. Cells are then fixed with 1%, 2%, 3% or 4% paraformaldehyde (PFA) for 15 min. Cells are incubated with 40 nM antibody conjugated Qdots for 45 min. Cells are imaged on an inverted Zeiss LSM 710 Confocal Microscope at 8 bits using 5 channels and 512 x 512 pixel resolution. Stack slices are at 200 nm intervals. Cells are excited with a 405 nm laser at 17%-22% laser power using a 63x apochromat 1.4 NA oil-immersion objective. Fluorescence is collected with the 32-channel Quasar multichannel photomultiplier tube. We used 525/30 nm, 565/30 nm, 605/30 nm, 655/30 nm and 705/30 nm emission filters with a maximum channel signal bleed of 6.4%. (Supplemental figure S8 and Table S9)

SDS-PAGE Antibody Quantification. MINI PROTEAN TGX 4-12% Bis-Tris gels (Biorad, Hercules, CA) and Laemmli sample buffer (Biorad, Hercules, CA) with 5% β-mercaptoethanol were used for the reduction of quantum dot-antibody conjugates. Briefly, Laemmli sample buffer, 1X Tris/Glycine/sodium dodecyl sulfate running buffer, β-mercaptoethanol (in reduced samples only) and each Qdot-antibody sample were mixed, according to standard SDS-PAGE protocols [107]. Samples were heated to 95°C for 15 min, centrifuged for 30 s and vortexed gently, and loaded into the gels using 10 µL per well. Gels wer run for 30 min at 200 V in 1X running buffer (900 mL of DI water and 100 mL SDS running buffer). Proteins separated by gel electrophoresis were visualized via overnight Commassie blue staining. The protein bands were visualized in gels using a standard gel doc XR system (Biorad, Hercules, CA) and analyzed using FIJI software, ImageJ (NIH, Bethesda, MD).

Dynamic Light Scattering. The Qdots-Ab size distribution was measured by dynamic light scattering (DLS, Zetasizer Nano ZS, Malvern Instruments, UK) equipped with a monochromatic coherent 4 mW 633 nm He-Ne laser. All measurements were performed triplicate in disposable cuvettes. Samples were vortex at 25 °C, 30 min prior to imaging.

Colocalization analysis. Images were deconvoluted using Autoquant X blind deconvolution algorithm. The co-localization analysis was performed using the plugin, Just Another Colocalization Plugin (JaCoP), which is available through the open source, ImageJ (NIH, Bethesda, MD) distribution package, FIJI [108]. Colocalization was estimated using Pearson's correlation coefficient (PC) [82] and thresholded Manders' coefficients [109]. PC checks for a linear correlation between localization and pixel intensity [82]. Costes thresholding evaluates the significance of the predicted PC via image scrambling, randomization, and PC calculation [83]. Thresholding is a common technique in colocalization analysis and is used to determine excluded pixels. We also present the non-thresholded data to evaluate the efficacy of the Costes approach. For each analysis we examined five images and reported colocalization if 60% (3/5) or more images give colocalization values (Table 1 x- and y-axes). Adding the z-axis of the images gives higher levels of colocalization due to the lower resolution available using this axis (Table S7).

Conclusions

Angiogenesis is critical to over 70 diseases[110]; therefore, these multiplexed Qdot probes could be used to insight into the roles of receptors in angiogenesis. More specifically, these probes can improve our understanding of angiogenic receptor distribution and dimerization by labeling cells and tissues, in vitro[12, 13]; cells isolated from blood or tissue, ex vivo [15, 16]; and fixed tumor biopsy tissue, indeed, we showed that multiplexed Qdot imaging can directly map angiogenic receptor distribution. We observed that VEGFR1 was primarily localized intracellularly; VEGFR2 & VEGFR3 were distributed evenly across plasma membrane, cytosol, and nuclear compartments; NRP1 was primarily on plasma membrane, and NRP2 was primarily in the nucleus. Translocation between cellular compartments is a known regulatory mechanism for receptor signaling, in particular tyrosine kinase receptor signaling[111, 112]; however, the functional consequences are not fully delineated [113-115]. Therefore, these multiplexed Qdots can be applied to image and functionally map angiogenic receptor partitioning. Additionally, receptor dimerization and complex formation regulates signal transduction[96, 116, 117]. Our co-localization analysis showed strong VEGFR1-R2, R2-R3, and N1-R2 co-localization, and possible R1-R3 and R3-N1 complexes. So these multiplexed Qdots can be further extended to further delineate how angiogenic receptor complexes regulate signaling.

Altogether, this work demonstrated the use of five different Qdot probes to simultaneously label and measure colocalization of five different angiogenic receptors on the cell surface. We measured the toxicity of the Qdots, observing that toxicity was correlated with Qdot size. We then tested different buffers to decrease toxicity. These experiments help move towards a

consensus on a standardized, robust protocol for antibody receptor labeling. Future studies should combine these probes with our previously developed Qdot calibration beads[118] to achieve multiplexed receptor profiling, quantitatively. The continuous development of novel labeling methods[119], and of more biocompatible materials such as silicon-based Qdots[120] will enhance the use of Qdots in basic science research and medical applications.

Author Contributions

P.I.I. and F.L.M. conceived this research project. P.I.I. and F.L.M analyzed the results and wrote the manuscript. F.L.M, designed and carried out experiments. P.L helped in the preliminary experiments and the graphic design of the table of contents. All authors have given approval to the final version of the manuscript.

Acknowledgements

We would like to the American Cancer Society, Illinois Division Basic Research Grant (282802), National Science Foundation-CBET Grant (1512598), and Mexico's National Council of Science and Technology (CONACyT) for funding support. We also would like to thank Dr. Mayandi Sivaguru (Shiv) for his help with the confocal microscope images and Audra Storm for her help with the confocal image colocalization analysis. The authors declare that there are no conflicts of interest.

Abbreviations

Qdot – Quantum dots; VEGFR1 - Vascular endothelial growth factor receptor-1; VEGFR2 - Vascular endothelial growth factor receptor-2; VEGFR3 - Vascular endothelial growth factor receptor-3; NRP1 – Neuropilin receptor-1; NRP2 – Neuropilin receptor-2; HUVEC – Human umbilical vein endothelial cells; SDS-PAGE - Sodium dodecyl sulfate polyacrylamide gel electrophoresis; FRET - Förster resonance energy transfer, TEM – Transmission electron microscope.

Notes and references

[a] Department of Bioengineering, University of Illinois at Urbana-Champaign, Urbana, IL, USA.
[b] Atlas Wearables, Austin, TX, USA.

†Corresponding Author
University of Illinois Urbana-Champaign
Department of Bioengineering
1304 W Springfield Avenue,
3235 Digital Computer Laboratory
Urbana, IL 61801
Tel 217-244-2651
pii@illinois.edu
http://publish.illinois.edu/systemsbio

The authors declare no competing financial interest.

Funding Sources:

American Cancer Society, Illinois Division Basic Research Grant (282802), NSF CBET (1512598), Mexico's National Council of Science and Technology (CONACyT)

Electronic Supplementary Information (ESI) available:

Additional information of Qdot size, spectra, images of HUVEC, HDFa cells, confocal microscopy setting and colocalization analysis results are included in the supporting information materials. This material is available free of charge. See DOI: 10.1039/b000000x/

References

1. T. Hunter, *Philosophical Transactions of the Royal Society of London. Series B: Biological Sciences*, 1998, **353**, 583-605.
2. R. M. Drenan, R. Nashmi, P. Imoukhuede, H. Just, S. McKinney and H. A. Lester, *Molecular pharmacology*, 2008, **73**, 27-41.
3. R. Nashmi, M. E. Dickinson, S. McKinney, M. Jareb, C. Labarca, S. E. Fraser and H. A. Lester, *The Journal of Neuroscience*, 2003, **23**, 11554-11567.
4. F. J. Moss, P. I. Imoukhuede, K. Scott, J. Hu, J. L. Jankowsky, M. W. Quick and H. A. Lester, *J Gen Physiol*, 2009, **134**, 489-521.
5. R. Srinivasan, R. Pantoja, F. Moss, E. D. W. Mackey, C. Son, J. Miwa and H. Lester, *The Journal of General Physiology*, 2011, **137**, 59-79.
6. H. Just, H. Sitte, J. Schmid, M. Freissmuth and O. Kudlacek, *Journal of Biological Chemistry*, 2004, **279**, 6650-6657.
7. P. I. Imoukhuede, F. J. Moss, D. J. Michael, R. H. Chow and H. A. Lester, *Biophys J*, 2009, **96**, 2949-2960.
8. B. Khakh, J. Fisher, R. Nashmi, D. Bowser and H. Lester, *The Journal of Neuroscience*, 2005, **25**, 6911-6920.
9. M. Backer and J. Backer, *Theranostics*, 2012, **2**, 502-515.
10. M. V. Backer, Z. Levashova, V. Patel, B. T. Jehning, K. Claffey, F. G. Blankenberg and J. M. Backer, *Nat Med*, 2007, **13**, 504-509.
11. Z. Levashova, M. Backer, C. V. Hamby, J. Pizzonia, J. M. Backer and F. G. Blankenberg, *Journal of Nuclear Medicine*, 2010, **51**, 959-966.
12. P. I. Imoukhuede and A. S. Popel, *Exp Cell Res*, 2011, **317**, 955-965.
13. S. Chen, X. Guo, O. Imarenezor and P. I. Imoukhuede, *Cellular and Molecular Bioengineering*, 2015, DOI: 10.1007/s12195-015-0411-x, 1-21.
14. P. I. Imoukhuede and A. S. Popel, *PLoS One*, 2012, **7**, e44791.
15. P. I. Imoukhuede, A. O. Dokun, B. H. Annex and A. S. Popel, *Am J Physiol Heart Circ Physiol*, 2013, **4**, H1085-1093.
16. P. I. Imoukhuede and A. S. Popel, *Cancer Medicine*, 2014, **3**, 225-244.
17. S. D. Finley, M. O. Engel-Stefanini, P. I. Imoukhuede and A. S. Popel, *BMC Syst Biol*, 2011, **5**, 193.
18. S. Finley and A. Popel, *Journal of the National Cancer Institute*, 2013, **105**, 802-811.
19. S. D. Finley, M. Dhar and A. S. Popel, *Frontiers in Oncology*, 2013, **3**.
20. J. C. Weddell and P. I. Imoukhuede, *PLoS ONE*, 2014, **9**, e97271.
21. Y. Sugiyama, I. Kawabata, K. Sobue and S. Okabe, *Nat Meth*, 2005, **2**, 677-684.
22. C.-S. Chiu, K. Jensen, I. Sokolova, D. Wang, M. Li, P. Deshpande, N. Davidson, I. Mody, M. W. Quick, S. R. Quake and H. A. Lester, *J. Neurosci.*, 2002, **22**, 10251-10266.
23. P. Schroeter, A. Sablotzki and D. Riemann, *Methods Mol Biol*, 2007, **378**, 71-81.
24. W. D. Hanley, S. L. Napier, M. M. Burdick, R. L. Schnaar, R. Sackstein and K. Konstantopoulos, *FASEB J.*, 2005, DOI: 10.1096/fj.05-4574fje, 05-4574fje.

25. R. J. Byers and E. R. Hitchman, *Progress in Histochemistry and Cytochemistry*, 2011, **45**, 201-237.
26. Y. Wu, S. K. Campos, G. P. Lopez, M. A. Ozbun, L. A. Sklar and T. Buranda, *Analytical Biochemistry*, 2007, **364**, 180-192.
27. N. O. Dantas, F. Qu, R. S. Silva and P. C. Morais, *The Journal of Physical Chemistry B*, 2002, **106**, 7453-7457.
28. Z. Hens, D. Vanmaekelbergh, E. J. A. J. Stoffels and H. van Kempen, *Physical Review Letters*, 2002, **88**, 236803.
29. W. C. W. Chan and S. Nie, *Science*, 1998, **281**, 2016-2018.
30. P. K. Chattopadhyay, D. A. Price, T. F. Harper, M. R. Betts, J. Yu, E. Gostick, S. P. Perfetto, P. Goepfert, R. A. Koup, S. C. De Rosa, M. P. Bruchez and M. Roederer, *Nat Med*, 2006, **12**, 972-977.
31. T. Y. Rakovich, O. K. Mahfoud, B. M. Mohamed, A. Prina-Mello, K. Crosbie-Staunton, T. Van Den Broeck, L. De Kimpe, A. Sukhanova, D. Baty, A. Rakovich, S. A. Maier, F. Alves, F. Nauwelaers, I. Nabiev, P. Chames and Y. Volkov, *ACS Nano*, 2014, **8**, 5682-5695.
32. M. V. Yezhelyev, A. Al-Hajj, C. Morris, A. I. Marcus, T. Liu, M. Lewis, C. Cohen, P. Zrazhevskiy, J. W. Simons, A. Rogatko, S. Nie, X. Gao and R. M. O'Regan, *Advanced Materials*, 2007, **19**, 3146-3151.
33. A. Albanese, P. S. Tang and W. C. W. Chan, *Annual Review of Biomedical Engineering*, 2012, **14**, 1-16.
34. A. M. Smith, S. Dave, S. Nie, L. True and X. Gao, *Expert Review of Molecular Diagnostics*, 2006, **6**, 231-244.
35. N. Chen, Y. He, Y. Su, X. Li, Q. Huang, H. Wang, X. Zhang, R. Tai and C. Fan, *Biomaterials*, 2012, **33**, 1238-1244.
36. X. Gao, Y. Cui, R. M. Levenson, L. W. K. Chung and S. Nie, *Nat Biotech*, 2004, **22**, 969-976.
37. F. T. Lee-Montiel and P. I. Imoukhuede, *Journal of Materials Chemistry B*, 2013, **1**, 6434.
38. K. Cho, X. Wang, S. Nie, Z. Chen and D. M. Shin, *Clinical Cancer Research*, 2008, **14**, 1310-1316.
39. C. H. J. Choi, C. A. Alabi, P. Webster and M. E. Davis, *Proceedings of the National Academy of Sciences*, 2010, **107**, 1235-1240.
40. B. Ballou, B. C. Lagerholm, L. A. Ernst, M. P. Bruchez and A. S. Waggoner, *Bioconjugate Chemistry*, 2003, **15**, 79-86.
41. S. J. Soenen, J. Demeester, S. C. De Smedt and K. Braeckmans, *Biomaterials*, 2012, **33**, 4882-4888.
42. C. E. Bradburne, J. B. Delehanty, K. Boeneman Gemmill, B. C. Mei, H. Mattoussi, K. Susumu, J. B. Blanco-Canosa, P. E. Dawson and I. L. Medintz, *Bioconjugate Chemistry*, 2013, **24**, 1570-1583.
43. A. M. Derfus, W. C. W. Chan and S. N. Bhatia, *Nano Letters*, 2003, **4**, 11-18.
44. Y. Xiao, S. Forry, X. Gao, R. D. Holbrook, W. Telford and A. Tona, *Journal of Nanobiotechnology*, 2010, **8**, 13.
45. M. M. Barroso, *Journal of Histochemistry & Cytochemistry*, 2011, **59**, 237-251.
46. B. D. Chithrani and W. C. W. Chan, *Nano Letters*, 2007, **7**, 1542-1550.
47. A. Al-Ali, N. Singh, B. Manshian, T. Wilkinson, J. Wills, G. J. Jenkins and S. H. Doak, *Toxicology Research*, 2015, **4**, 623-633.
48. B. J. Roxworthy, M. T. Johnston, F. T. Lee-Montiel, R. H. Ewoldt, P. I. Imoukhuede and K. C. Toussaint, Jr., *PLoS ONE*, 2014, **9**, e93929.
49. in *The MAK-Collection for Occupational Health and Safety*, Wiley-VCH Verlag GmbH & Co. KGaA, 2002, DOI: 10.1002/3527600418.mb2662822e0020.
50. A. W. Gross and H. F. Lodish, *Journal of Biological Chemistry*, 2006, **281**, 2024-2032.
51. H. Gao, Z. Yang, S. Zhang, S. Cao, S. Shen, Z. Pang and X. Jiang, *Sci. Rep.*, 2013, **3**.
52. M. S. Goldstein, *Journal of Biological Chemistry*, 1952, **199**, 923-928.
53. Hardman R, *Environ Health Perspect*, 2006, **114**, 165-172.
54. K. M. Tsoi, Q. Dai, B. A. Alman and W. C. W. Chan, *Accounts of Chemical Research*, 2012, DOI: 10.1021/ar300040z.
55. P. Wigge and H. T. McMahon, *Trends in Neurosciences*, 1998, **21**, 339-344.
56. C. Lüscher, H. Xia, E. C. Beattie, R. C. Carroll, M. von Zastrow, R. C. Malenka and R. A. Nicoll, *Neuron*, 1999, **24**, 649-658.
57. M.-Y. Xiao, Q. Zhou and R. A. Nicoll, *Neuropharmacology*, 2001, **41**, 664-671.
58. Y. Williams, S. Byrne, M. Bashir, A. Davies, Á. Whelan, Y. Gun'Ko, D. Kelleher and Y. Volkov, *Journal of Microscopy*, 2008, **232**, 91-98.
59. S. Mittar, C. Ulyatt, G. J. Howell, A. F. Bruns, I. Zachary, J. H. Walker and S. Ponnambalam, *Experimental Cell Research*, 2009, **315**, 877-889.
60. Z. Zhang, K. Neiva, M. Lingen, L. Ellis and J. Nor, *Cell Death and Differentiation*, 2010, DOI: 10.1038/cdd.2009.152, 499-512.
61. H. M. Jopling, G. J. Howell, N. Gamper and S. Ponnambalam, *Biochemical and Biophysical Research Communications*, 2011, **410**, 170-176.
62. H. M. Jopling, A. F. Odell, N. M. Hooper, I. C. Zachary, J. H. Walker and S. Ponnambalam, *Arteriosclerosis, Thrombosis, and Vascular Biology*, 2009, **29**, 1119-1124.
63. M. G. Lampugnani, F. Orsenigo, M. C. Gagliani, C. Tacchetti and E. Dejana, *The Journal of Cell Biology*, 2006, **174**, 593-604.
64. L. C. Ewan, H. M. Jopling, H. Jia, S. Mittar, A. Bagherzadeh, G. J. Howell, J. H. Walker, I. C. Zachary and S. Ponnambalam, *Traffic*, 2006, **7**, 1270-1282.
65. A. Gampel, L. Moss, M. C. Jones, V. Brunton, J. C. Norman and H. Mellor, *Blood*, 2006, **108**, 2624-2631.
66. R. Bhattacharya, N. Kang-Decker, D. A. Hughes, P. Mukherjee, V. Shah, M. A. McNiven and D. Mukhopadhyay, *The FASEB Journal*, 2005, **19**, 1692-1694.
67. I. Zachary, 2013.
68. D. Moyon, L. Pardanaud, L. Yuan, C. Bréant and A. Eichmann, *Development*, 2001, **128**, 3359-3370.
69. S. Koch, Laurens A. van Meeteren, E. Morin, C. Testini, S. Weström, H. Björkelund, S. Le Jan, J. Adler, P. Berger and L. Claesson-Welsh, *Developmental Cell*, 2014, **28**, 633-646.
70. D. R. Bielenberg, C. A. Pettaway, S. Takashima and M. Klagsbrun, *Experimental Cell Research*, 2006, **312**, 584-593.
71. Z. Gluzman-Poltorak, T. Cohen, Y. Herzog and G. Neufeld, *Journal of Biological Chemistry*, 2000, **275**, 18040-18045.
72. H. Chen, A. Chédotal, Z. He, C. S. Goodman and M. Tessier-Lavigne, *Neuron*, 1997, **19**, 547-559.
73. L. Yuan, D. Moyon, L. Pardanaud, C. Bréant, M. J. Karkkainen, K. Alitalo and A. Eichmann, *Development*, 2002, **129**, 4797-4806.
74. K. Bouvrée, I. Brunet, R. del Toro, E. Gordon, C. Prahst, B. Cristofaro, T. Mathivet, Y. Xu, J. Soueid, V. Fortuna, N. Miura, M.-S. Aigrot, C. H. Maden, C. Ruhrberg, J. L. Thomas and A. Eichmann, *Circulation Research*, 2012, **111**, 437-445.
75. M. J. Karkkainen, A. Saaristo, L. Jussila, K. A. Karila, E. C. Lawrence, K. Pajusola, H. Bueler, A. Eichmann, R. Kauppinen, M. I. Kettunen, S. Ylä-Herttuala, D. N. Finegold, R. E. Ferrell and K. Alitalo, *Proceedings of the National Academy of Sciences*, 2001, **98**, 12677-12682.
76. L. Verlinden, C. Kriebitzsch, I. Beullens, B. K. Tan, G. Carmeliet and A. Verstuyf, *Bone*, 2013, **55**, 465-475.
77. M. Torigoe, K. Yamauchi, A. Tamada, I. Matsuda, A. Aiba, V. Castellani and F. Murakami, *European Journal of Neuroscience*, 2013, **37**, 1573-1583.
78. H. Fujita, B. Zhang, K. Sato, J. Tanaka and M. Sakanaka, *Brain Research*, 2001, **914**, 1-14.
79. A. M. Jubb, L. A. Strickland, S. D. Liu, J. Mak, M. Schmidt and H. Koeppen, *The Journal of Pathology*, 2012, **226**, 50-60.
80. M. Caunt, J. Mak, W.-C. Liang, S. Stawicki, Q. Pan, R. K. Tong, J. Kowalski, C. Ho, H. B. Reslan, J. Ross, L. Berry, I. Kasman, C. Zlot, Z. Cheng, J. Le Couter, E. H. Filvaroff, G. Plowman, F. Peale, D. French, R. Carano, Alexander W. Koch, Y. Wu, R. J. Watts, M. Tessier-Lavigne and A. Bagri, *Cancer Cell*, 2008, **13**, 331-342.
81. Y. Cao, L. H. Hoeppner, S. Bach, G. E, Y. Guo, E. Wang, J. Wu, M. J. Cowley, D. K. Chang, N. Waddell, S. M. Grimmond, A. V. Biankin, R. J. Daly, X. Zhang and D. Mukhopadhyay, *Cancer Research*, 2013, **73**, 4579-4590.
82. E. M. M. Manders, F. J. Verbeek and J. A. Aten, *Journal of Microscopy*, 1993, **169**, 375-382.

83. S. V. Costes, D. Daelemans, E. H. Cho, Z. Dobbin, G. Pavlakis and S. Lockett, *Biophysical Journal*, 2004, **86**, 3993-4003.
84. A. Ahmed, C. Dunk, D. Kniss and M. Wilkes, *Laboratory investigation; a journal of technical methods and pathology*, 1997, **76**, 779-791.
85. N. Rahimi, V. Dayanir and K. Lashkari, *Journal of Biological Chemistry*, 2000, **275**, 16986-16992.
86. B. Bussolati, C. Dunk, M. Grohman, C. D. Kontos, J. Mason and A. Ahmed, *The American Journal of Pathology*, 2001, **159**, 993-1008.
87. C. Dunk and A. Ahmed, *The American Journal of Pathology*, 2001, **158**, 265-273.
88. F. Mac Gabhann and A. S. Popel, *Biophysical Chemistry*, 2007, **128**, 125-139.
89. R. L. Kendall, G. Wang and K. A. Thomas, *Biochemical and Biophysical Research Communications*, 1996, **226**, 324-328.
90. P.-E. Neagoe, C. Lemieux and M. G. Sirois, *Journal of Biological Chemistry*, 2005, **280**, 9904-9912.
91. M. Autiero, J. Waltenberger, D. Communi, A. Kranz, L. Moons, D. Lambrechts, J. Kroll, S. Plaisance, M. De Mol, F. Bono, S. Kliche, G. Fellbrich, K. Ballmer-Hofer, D. Maglione, U. Mayr-Beyrle, M. Dewerchin, S. Dombrowski, D. Stanimirovic, P. Van Hummelen, C. Dehio, D. J. Hicklin, G. Persico, J.-M. Herbert, D. Communi, M. Shibuya, D. Collen, E. M. Conway and P. Carmeliet, *Nat Med*, 2003, **9**, 936-943.
92. M. J. Cudmore, P. W. Hewett, S. Ahmad, K.-Q. Wang, M. Cai, B. Al-Ani, T. Fujisawa, B. Ma, S. Sissaoui, W. Ramma, M. R. Miller, D. E. Newby, Y. Gu, B. Barleon, H. Weich and A. Ahmed, *Nat Commun*, 2012, **3**, 972.
93. P. I. Imoukhuede and A. S. Popel, *Experimental Cell Research*, 2011, **317**, 955-965.
94. J. Dixelius, T. Mäkinen, M. Wirzenius, M. J. Karkkainen, C. Wernstedt, K. Alitalo and L. Claesson-Welsh, *Journal of Biological Chemistry*, 2003, **278**, 40973-40979.
95. A. Alam, J.-P. Herault, P. Barron, B. Favier, P. Fons, N. Delesque-Touchard, I. Senegas, P. Laboudie, J. Bonnin, C. Cassan, P. Savi, B. Ruggeri, P. Carmeliet, F. Bono and J.-M. Herbert, *Biochemical and Biophysical Research Communications*, 2004, **324**, 909-915.
96. I. Nilsson, F. Bahram, X. Li, L. Gualandi, S. Koch, M. Jarvius, O. Soderberg, A. Anisimov, I. Kholova, B. Pytowski, M. Baldwin, S. Yla-Herttuala, K. Alitalo, J. Kreuger and L. Claesson-Welsh, *EMBO J*, 2010, **29**, 1377-1388.
97. S. Soker, S. Takashima, H. Q. Miao, G. Neufeld and M. Klagsbrun, *Cell*, 1998, **92**, 735-745.
98. S. Soker, H.-Q. Miao, M. Nomi, S. Takashima and M. Klagsbrun, *Journal of Cellular Biochemistry*, 2002, **85**, 357-368.
99. C. Boscher and I. Nabi, in *Caveolins and Caveolae*, eds. J.-F. Jasmin, P. Frank and M. Lisanti, Springer US, 2012, vol. 729, ch. 3, pp. 29-50.
100. C. Caliceti, L. Zambonin, B. Rizzo, D. Fiorentini, F. Vieceli Dalla Sega, S. Hrelia and C. Prata, *BioMed Research International*, 2014, **2014**, 13.
101. E. Saulle, R. Riccioni, S. Coppola, I. Parolini, D. Diverio, V. Riti, G. Mariani, S. Laufer, M. Sargiacomo and U. Testa, *British Journal of Haematology*, 2009, **145**, 399-411.
102. S. T. Low-Nam, K. A. Lidke, P. J. Cutler, R. C. Roovers, P. M. P. van Bergen en Henegouwen, B. S. Wilson and D. S. Lidke, *Nat Struct Mol Biol*, 2011, **18**, 1244-1249.
103. S. Yang, M. A. Raymond-Stintz, W. Ying, J. Zhang, D. S. Lidke, S. L. Steinberg, L. Williams, J. M. Oliver and B. S. Wilson, *Journal of cell science*, 2007, **120**, 2763-2773.
104. K. Simons and M. J. Gerl, *Nature reviews Molecular cell biology*, 2010, **11**, 688-699.
105. Y. Chen, C. Short, A. M. Halász and J. S. Edwards, *Electronic proceedings in theoretical computer science*, 2013, **2013**, 37.
106. H. Yuan, J. Li, G. Bao and S. Zhang, *Physical review letters*, 2010, **105**, 138101.
107. A. L. Shapiro, E. Viñuela and J. V. Maizel Jr, *Biochemical and Biophysical Research Communications*, 1967, **28**, 815-820.
108. J. Schindelin, I. Arganda-Carreras, E. Frise, V. Kaynig, M. Longair, T. Pietzsch, S. Preibisch, C. Rueden, S. Saalfeld, B. Schmid, J.-Y. Tinevez, D. J. White, V. Hartenstein, K. Eliceiri, P. Tomancak and A. Cardona, *Nat Meth*, 2012, **9**, 676-682.
109. E. M. Manders, J. Stap, G. J. Brakenhoff, R. van Driel and J. A. Aten, *Journal of Cell Science*, 1992, **103**, 857-862.
110. P. Carmeliet, *Nature*, 2005, **438**, 932-936.
111. M. Miaczynska, *Cold Spring Harbor Perspectives in Biology*, 2013, **5**.
112. Y. Du, J. Hsu, Y.-N. Wang and M.-C. Hung, in *Receptor Tyrosine Kinases: Structure, Functions and Role in Human Disease*, eds. D. L. Wheeler and Y. Yarden, Springer New York, 2015, DOI: 10.1007/978-1-4939-2053-2_5, ch. 5, pp. 77-109.
113. H. G. J. B. A. F. Z. I. W. J. H. P. S. Mittar S Ulyatt C and B. A. Mittar S Howell GJ, Zachary I, Walker JH, Ponnambalam S, Ulyatt C, *Exp Cell Res*, 2009, **314**, 877-889.
114. Z. Zhang, N. KG, L. MW, E. LM and N. JE, *Cell Death Differ*, 2010, **17**, 499-512.
115. A. Bruns, L. Bao, J. Walker and S. Ponnambalam, *Biochemical Society Transactions*, 2009, **37**, 1193-1197.
116. L. Chen, L. Novicky, M. Merzlyakov, T. Hristov and K. Hristova, *Journal of the American Chemical Society*, 2010, **132**, 3628-3635.
117. M. P. Steinkamp, S. T. Low-Nam, S. Yang, K. A. Lidke, D. S. Lidke and B. S. Wilson, *Molecular and Cellular Biology*, 2014, **34**, 965-977.
118. F. Lee-Montiel and P. I. Imoukhuede, *Journal of Materials Chemistry B*, 2013, DOI: 10.1039/c3tb20904k.
119. Y. Xing, Q. Chaudry, C. Shen, K. Y. Kong, H. E. Zhau, L. W. Chung, J. A. Petros, R. M. O'Regan, M. V. Yezhelyev, J. W. Simons, M. D. Wang and S. Nie, *Nat. Protocols*, 2007, **2**, 1152-1165.
120. J. Liu, F. Erogbogbo, K.-T. Yong, L. Ye, J. Liu, R. Hu, H. Chen, Y. Hu, Y. Yang, J. Yang, I. Roy, N. A. Karker, M. T. Swihart and P. N. Prasad, *ACS Nano*, 2013, **7**, 7303-7310.